JOURNAL OF
SYNCHROTRON
RADIATION

ISSN 1600-5775

Optimization of a phase-space beam position and size monitor for low-emittance light sources

Nazanin Samadi,[a] Xianbo Shi[b]* and Dean Chapman[c]

[a]Physics and Engineering Physics, University of Saskatchewan, 116 Science Place, Saskatoon, SK S7N5E2, Canada,
[b]Advanced Photon Source, Argonne National Laboratory, 9700 South Cass Avenue, Lemont, IL 60439, USA, and
[c]Canadian Light Source, 44 Innovation Boulevard, Saskatoon, SK S7N2V3, Canada.
*Correspondence e-mail: xshi@aps.anl.gov

Received 6 June 2019
Accepted 29 July 2019

Edited by S. M. Heald, Argonne National Laboratory, USA

Keywords: beam position and size monitor; phase space; diagnostics and feedback; ray-tracing simulation; diffraction-limited storage rings.

The recently developed vertical phase-space beam position and size monitor (ps-BPM) system has proven to be able to measure the electron-source position, angle, size and divergence simultaneously in the vertical plane at a single location of a beamline. The optimization of the ps-BPM system is performed by ray-tracing simulation to maximize the instrument sensitivity and resolution. The contribution of each element is studied, including the monochromator, the *K*-edge filter, the detector and the source-to-detector distance. An optimized system is proposed for diffraction-limited storage rings, such as the Advanced Photon Source Upgrade project. The simulation results show that the ps-BPM system can precisely monitor the source position and angle at high speed. Precise measurements of the source size and divergence will require adequate resolution with relatively longer integration time.

1. Introduction

The new-generation synchrotron facilities are being designed and built to achieve an ultra-small emittance utilizing multi-bend achromat (MBA) lattices (Einfeld *et al.*, 2014).

Measurements of electron-beam position and size are challenging and important for the operation of these new light sources (Eriksson *et al.*, 2014; Tavares *et al.*, 2014). The existing and planned diagnostics for measuring the source size for the MBA sources include pinhole imaging (Elleaume *et al.*, 1995; Thomas *et al.*, 2010), π-polarization imaging (Andersson *et al.*, 2008; Breunlin & Andersson, 2016), double-slit interferometry (Mitsuhashi, 1999; Naito & Mitsuhashi, 2006; Corbett *et al.*, 2016) and Kirkpatrick–Baez (KB) mirrors (Renner *et al.*, 1996; Zhu *et al.*, 2018). Most of these systems use dedicated bending magnet (BM) beamlines. The larger size of the BM source, resulting from larger beta function, compared with other locations in the lattice, allows for more precise measurements.

The pinhole-camera measurement with X-rays is the simplest system, but for source sizes of less than 10 µm it is impractical because diffraction by the pinhole complicates extracting information about the source size from the image. The double-slit interferometry system has better resolution compared with pinhole imaging because the blurring caused by the source size reduces the contrast. In this case, the contrast is a measure of the source size, which does not rely on direct imaging. These measurements are photon hungry, and wavefront distortions caused by optical components can result in inaccurate source-size measurements.

The π-polarization technique, another interference-based method, utilizes the out-of-orbital plane vertical (π) polarization of the BM beam and, similar to the double-slit method,

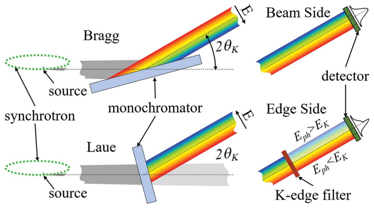

depends on source size to reduce the intensity 'null' at the midplane.

KB mirror systems use two cylindrical mirrors, one focusing the photon beam horizontally and the other focusing it vertically onto a CCD to measure the source size. In order to beat the diffraction limit, the KB mirror system must use short-wavelength synchrotron radiation.

In all of these methods, knowledge of the point-spread function of the detection system is essential for the source-size deconvolution. The contribution from the detector resolution has to be minimized for small source-size measurements.

The vertical phase-space beam position and size monitor (ps-BPM) system (Samadi *et al.*, 2015, 2019) developed at the Canadian Light Source (CLS) has demonstrated the ability to measure the source size and divergence, as well as the source position and angle in the vertical plane, at a single location and time. In this article, we will report on the process of optimizing the ps-BPM system for ultra-small electron-source-size measurements and provide an example for the Advanced Photon Source Upgrade (APS-U) project (Borland *et al.*, 2018).

1.1. ps-BPM system

A ps-BPM system, as shown in Fig. 1, contains a crystal-based monochromator, a *K*-edge filter and an area detector. The monochromator is tuned to the photon energy of the *K*-edge of the filter element. The system utilizes the large horizontal photon fan of the BM beamline to simultaneously measure the direct beam (unfiltered beam) and the part going through the *K*-edge filter (filtered beam). These beams include both σ and π polarizations, and the polarization effect is negligible in the analysis.

The natural vertical opening angle of the photon beam (Schwinger, 1949) provides a Gaussian-type profile for the unfiltered side of the beam at photon energies well above the critical energy of the BM source. It is the central location and width of this unfiltered beam that is used in the data analysis. The photon-beam opening angle also provides a range of incident angles onto the monochromator crystal. This range of angles can give an energy range about the central *K*-edge energy. The *K*-edge will introduce a step-type function through this energy range. The location and width of the *K*-edge are used in the analysis of the filtered data.

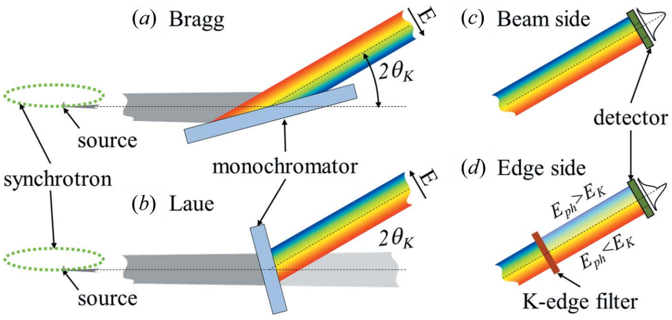

Figure 1
Schematic of the ps-BPM system including a Bragg (*a*) or Laue (*b*) crystal monochromator, a *K*-edge filter in (*d*), and a detector which records both the unfiltered beam side (*c*) and filtered edge side (*d*) of the beam.

The vertical profiles of the filtered and unfiltered beams contain the information of the electron-source position, angle, size and divergence (Samadi *et al.*, 2015). The position of the *K*-edge location in the filtered beam, $y_{\rm edge}$, is a direct measure of the electron-source position, $y_{\rm eSource}$. In other words,

$$y_{\rm eSource} = y_{\rm edge}. \tag{1}$$

The electron-source size, $\sigma_{y_{\rm eSource}}$, can be extracted from the spatial width of the measured *K*-edge on the detector, $\sigma_{\rm edge}$, by (Samadi *et al.*, 2019)

$$\sigma_{y_{\rm eSource}} = \left[\left(\sigma_{\rm edge}\right)^2 - \left(D\sigma_{y'_{K\,{\rm edge}}}\right)^2 - \left(D\sigma_{y'_{\rm mono}}\right)^2\right]^{1/2}, \tag{2}$$

where D is the source-to-detector distance, $\sigma_{y'_{K\,{\rm edge}}}$ is the natural width of the *K*-edge of the filter element translated from an energy width to an angular width (see Section 2) and $\sigma_{y'_{\rm mono}}$ is the angular acceptance of the monochromator (Warren, 1969; Zachariasen, 1945). The electron-source emission angle, $y'_{\rm eSource}$, and divergence, $\sigma_{y'_{\rm eSource}}$, can be obtained from the simultaneously measured unfiltered beam position, $y_{\rm beam}$, and width, $\sigma_{\rm beam}$, by

$$y'_{\rm eSource} = \frac{1}{D}\left(y_{\rm beam} - y_{\rm edge}\right) \tag{3}$$

and

$$\sigma_{y'_{\rm eSource}} = \frac{1}{D}\left[\left(\sigma_{\rm beam}\right)^2 - \left(\sigma_{y_{\rm eSource}}\right)^2 - \left(D\sigma_{y'_{\rm Ph}}\right)^2\right]^{1/2}, \tag{4}$$

respectively, where $\sigma_{y'_{\rm ph}}$ is the natural opening angle of the photon beam (Schwinger, 1949). In the following sections, each term in equations (1)–(4) will be quantitatively analyzed with numerical simulation.

1.2. Simulation tools and method

The system measures the beam along the direction perpendicular to the orbital plane, which is also the diffraction plane of the monochromator that is typically vertical. Taking this direction, the system can be described by the propagation of the photon beam through phase space, which minimally includes three dimensions, the energy, E, the vertical spatial coordinate, y, and the vertical angular coordinate, y'. To describe the system in sufficient resolution each dimension needs at least a grid size of 10^3, which gives a total matrix size of 10^9. To reduce the computation effort, Monte Carlo based geometrical ray tracing is used for this work.

All simulations are performed using the *ShadowOui* program (Rebuffi & Sánchez del Río, 2016) in the *OASYS* (Rebuffi & Sanchez del Rio, 2017) environment. In *ShadowOui*, each type of source and optical element is defined as an individual 'widget'. The BM source is simulated using the 'Bending Magnet' widget, which requires input of electron-source size, electron emittance ($\propto \sigma_{y_{\rm eSource}}\sigma_{y'_{\rm eSource}}$) and magnetic field of the BM. A BM point source (zero emittance) (PS) can be created by setting both $\sigma_{y_{\rm eSource}}$ and $\sigma_{y'_{\rm eSource}}$ to zero, which is used to generate the photon-beam distribution representing the single-electron emission or single-electron point-spread function from the BM. The BM source includes both horizontal (σ) and vertical (π) polarization components; however, only about 4% of the total intensity is contained in the π polarization.

The monochromators considered in this work are single crystals in the Bragg and Laue geometry. All crystals are simulated using the 'Plane Crystal' widgets in *ShadowOui*, where the crystal Bragg angle is set to be auto-tuned to the K-edge energy, E_K, of the selected filter element.

The K-edge filter is the next optical element downstream of the monochromator. The built-in module in *ShadowOui* for filter absorption does not contain lifetime broadening for the K-edge spectrum, which is the main contributor to the edge width, $\sigma_{\rm edge}$, in real measurements. Therefore, a dedicated Python script was made inside the *OASYS* environment to simulate the filter absorption by assigning each ray an intensity scaling factor based on its photon energy and the transmission curve. The transmission through the filter is calculated by

$$T = \exp\left[-\frac{\mu}{\rho}(E)\rho t\right], \tag{5}$$

where $(\mu/\rho)(E)$ is the energy-dependent mass-attenuation coefficient around the K-edge of the filter, ρ is the concentration and t is the effective filter thickness. The K-edge spectrum depends on the core-level width, which is normally described by a Lorenz function (Babanov *et al.*, 1998). In this work, to be consistent with the experimental results (Samadi *et al.*, 2015), a Gaussian function is used.

A typical simulation to achieve sufficient statistics requires 5×10^7 to 5×10^8 rays, which is challenging to run and store as a single simulation. Therefore, a recursive loop is implemented to accumulate results of multiple runs (typically 100 to 3200), each of which contains 5×10^5 rays. The vertical photon-beam profiles are recorded as histograms that collect rays at the detector position. The histograms are weighted by the ray intensity which contains information on the crystal reflectivity and the filter transmission. The bin size of the histograms is a representation of the pixel size of the detector. The vertical profiles of the filtered beam, $I_{\rm filtered}(y)$, and the unfiltered beam, $I_0(y)$, are collected and stored for post analysis [see Fig. 2(*a*)].

The simulated photon-beam profiles are then analyzed based on the same data-analysis process developed for experimental results (Samadi *et al.*, 2019). The edge profile, $f_{\rm edge}(y)$, shown in Fig. 2(*b*), is obtained by

$$f_{\rm edge}(y) = \frac{{\rm d}\{-\ln[I_{\rm filtered}(y)/I_0(y)]\}}{{\rm d}y}. \tag{6}$$

The edge profile and the unfiltered beam profile are both fitted to a Gaussian function with widths of $\sigma_{\rm edge}$ and $\sigma_{\rm beam}$, and center positions, $y_{\rm edge}$ and $y_{\rm beam}$, respectively, given by

$$I_0(y) = A_0 \exp\left[-\frac{\left(y - y_{\rm beam}\right)^2}{2\sigma^2_{\rm beam}}\right] + A_1, \tag{7}$$

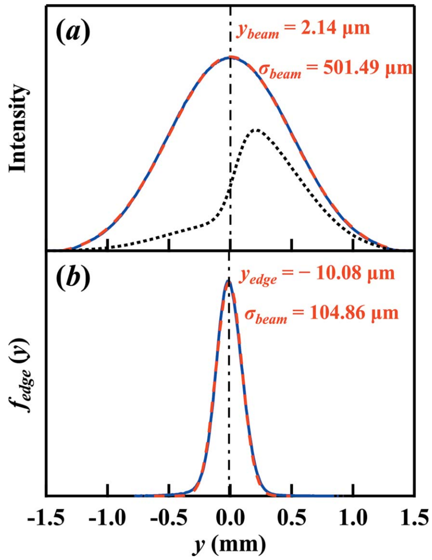

Figure 2
(*a*) The simulated vertical profiles of the filtered beam, $I_{\rm filtered}(y)$ (dotted curve), and the unfiltered beam, $I_0(y)$ (solid curve), and (*b*) the edge profile, $f_{\rm edge}(y)$ (solid curve), obtained from equation (6). The dashed curves in (*a*) and (*b*) are the Gaussian fitting of $I_0(y)$ and $f_{\rm edge}(y)$ using equations (7) and (8), respectively.

and

$$f_{\rm edge}(y) = B_0 \exp\left[-\frac{\left(y - y_{\rm edge}\right)^2}{2\sigma^2_{\rm edge}}\right] + B_1. \tag{8}$$

The position and angle at the electron-beam source are extracted from the fitted $y_{\rm beam}$ and $y_{\rm edge}$ values using equations (1) and (3), respectively. The electron-beam source size is obtained by deconvolving the edge width, $\sigma_{\rm edge,PS}$, of a zero-emittance point source from that of the BM source, $\sigma_{\rm edge,BM}$, with a finite electron-beam size, given by

$$\sigma_{y_{\rm eSource}} = \left(\sigma^2_{\rm edge,BM} - \sigma^2_{\rm edge,PS}\right)^{1/2}. \tag{9}$$

Comparing equation (9) with equation (2), the simulated $\sigma_{\rm edge,PS}$ term represents the total contribution of $D\sigma_{y'_{K\,\rm edge}}$ and $D\sigma_{y'_{\rm mono}}$. The electron-beam divergence is then obtained from the photon-beam widths for the BM source, $\sigma_{\rm beam,BM}$, and for the zero-emittance point source, $\sigma_{\rm beam,PS}$, by

$$\sigma_{y'_{\rm eSource}} = \frac{1}{D}\left(\sigma^2_{\rm beam,BM} - \sigma^2_{\rm beam,PS} - \sigma^2_{y_{\rm eSource}}\right)^{1/2}. \tag{10}$$

The simulated $\sigma_{\rm beam,PS}$ term represents $D\sigma_{y'_{\rm ph}}$ in equation (4). The simulation error is calculated as the standard deviation of results from 100 separate ray-tracing calculations unless otherwise specified.

2. Optimization process

The optimization process involves aspects of the system that determine its ability to best measure source properties. These factors include the monochromator, the K-edge filter, detector characteristics, and arrangement of these components (measurement geometry).

Two cases are considered: a BM at the CLS and a BM for the APS-U.

For the CLS, the simulation study is for a 1.354 T BM and an electron beam with $\sigma_{y_{\rm eSource}} = 52.7\ \mu{\rm m}$ and $\sigma_{y'_{\rm eSource}} = 6.35\ \mu{\rm rad}$ (Bergstrom & Vogt, 2008). Unless specified, all simulations were performed with a monochromator tuned to the barium K-edge energy (37.441 keV), a 35 mg cm^{-2} barium K-edge filter and a source-to-detector distance of $D = 10$ m.

2.1. Monochromator

The monochromator is one of the most critical components of a ps-BPM system. The effect of the monochromator and the choice of the K-edge filter are closely related to each other through the angle–energy dispersion from Bragg's law. The dispersion effect of the monochromator crystal projects the absorption-edge energy width, $\sigma_{E_{K\,{\rm edge}}}$, into an angular width, $\sigma_{y'_{K\,{\rm edge}}}$ (measured by the spatial width on the detector at distance D) through the relationship

$$\sigma_{y'_{K\,{\rm edge}}} = \frac{\tan\theta_K}{E_K}\sigma_{E_{K\,{\rm edge}}}, \tag{11}$$

where θ_K is the Bragg angle of the monochromator crystal at the filter K-edge energy, E_K. In general, to achieve small $\sigma_{y'_{K\,{\rm edge}}}$ requires a filter with small $\sigma_{E_{K\,{\rm edge}}}$, a high K-edge energy and a small Bragg angle. This section and Section 2.2 below show in detail how these terms contribute to the measurement.

There are several choices for the crystal material, reflection geometry and lattice planes that will now be considered.

2.1.1. Crystal material and geometry. Single-crystal materials are considered for the monochromator. High-quality semiconductor crystals are commonly available as a consequence of the semiconductor industry drive to improve device performance. Dynamical theory (Zachariasen, 1945) can be used to describe the diffraction properties of such crystals. Silicon is the most common monochromator crystal used for X-ray beamlines because of its availability, degree of perfection and ability to handle synchrotron-radiation heat loading.

The diffraction geometry from crystals falls into two broad categories. The reflection or Bragg geometry has lattice planes mostly parallel to the crystal's surface; X-rays impinge upon and diffract out of the same surface. In transmission or Laue geometry the lattice planes are mostly perpendicular to the crystal surface; X-rays impinge upon one surface and exit through another by diffracting through the crystal.

Laue geometry has two practical advantages over Bragg geometry because it allows a smaller footprint (a smaller crystal) and reduced thermal deformation from the photon-beam heat load. Nevertheless, based on the diffraction profiles [see Fig. 3(*a*)] calculated using the *XCRYSTAL* module (Sanchez del Rio *et al.*, 2015) in *XOP* (Sánchez del Río & Dejus, 2011), Bragg geometry is preferred owing to the higher reflectivity and narrower bandwidth compared with Laue geometry.

Intensive efforts are being dedicated to the studies of crystal quality and thermal mechanical design of monochromators, which are not in the scope of this work. We limit the following discussions to single Bragg silicon crystals and focus on the optical optimization of the ps-BPM system.

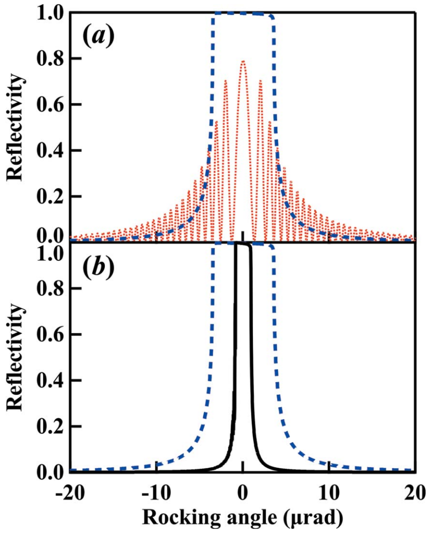

Figure 3
Diffraction profiles of the Si(111) reflection in the Bragg (dashed line) and Laue (dotted line) geometry and in the Si(440) Bragg reflection (solid line).

2.1.2. Crystal lattice planes. The intrinsic angular bandwidth of a monochromator, $\sigma_{y'_{\rm mono}}$, can be modeled using standard dynamical theory (Zachariasen, 1945). Reflection from high-indices planes [*e.g.* Si(440)] has smaller angular bandwidth, as shown in Fig. 3(*b*). This effect can be clearly seen in the DuMond diagrams (DuMond, 1937) shown in Fig. 4, where a zero-emittance BM source is monochromated by a Si(111) crystal [Fig. 4(*a*)] and a Si(440) crystal [Fig. 4(*b*)] to the barium K-edge energy. Assuming the photon beam is absorbed by a barium filter with a sharp edge ($\sigma_{E_{K\,{\rm edge}}} = 0$), the intrinsic bandwidth of the crystal is spatially projected onto the detector plane (the y axis in Fig. 4). The Si(440) reflection contributes to a much smaller edge width, yet gives a larger Bragg angle [steeper y versus energy slope in Fig. 4(*b*)]. This has the effect of limiting the energy range that the monochromator will cover with the photon-beam divergence from the source. A limited energy range is not ideal when the filter-

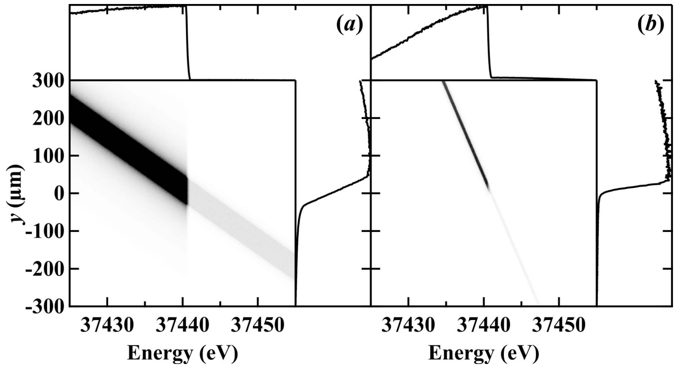

Figure 4
Simulated DuMond diagrams using a zero-emittance BM source that is diffracted by (*a*) a Si(111) and (*b*) a Si(440) crystal, and filtered by a barium filter with a sharp K-edge ($\sigma_{E_{K\,{\rm edge}}} = 0$).

Table 1
Barium K-edge width, $\sigma_{E_{K\,\mathrm{edge}}}$, and the equivalent angular width, $\sigma_{y'_{K\,\mathrm{edge}}}$, calculated using equation (11).

E_K = 37.441 keV	Si(111)	Si(220)	Si(311)	Si(440)
θ_K (°)	3.027	4.947	5.804	9.931
$\sigma_{E_{K\,\mathrm{edge}}}$ (eV)	5.6	5.6	5.6	5.6
$\sigma_{y'_{K\,\mathrm{edge}}}$ (μrad)	7.9	13.0	15.2	26.2

edge width, $\sigma_{E_{K\,\mathrm{edge}}}$, is non-zero based on equation (11). Table 1 shows the angular width of the barium K-edge in angle, $\sigma_{y'_{K\,\mathrm{edge}}}$, with different crystal reflections. For the same energy edge width ($\sigma_{E_{K\,\mathrm{edge}}}$ = 5.6 eV, or a FWHM of 13.2 eV assuming a Gaussian distribution) (Babanov *et al.*, 1998), a crystal with lower reflection indices is preferred.

2.2. *K*-edge filter

The choice of the K-edge filter determines the energy to be selected by the monochromator. Also, the K-edge width affects the ability to determine the source size [see equation (2)] as it needs to be accounted for in the overall edge-width measurement. Since the monochromator and energy will determine the flux from the source, the ability to accurately determine the center and width of the distribution will rely on the statistical fitting of the vertical profile of the beam. The same applies to the K-edge filter where a statistical fit to the edge location and width is performed. The flux for those measurements depends upon the K-edge filter element attenuation (μ/ρ), concentration (ρ) and thickness (t) [see equation (5)]. The product of concentration and thickness is commonly referred to as the projected concentration (mass per area) of the filter.

2.2.1. *K*-edge choice. The natural energy width of the K-edge of an element is dominated by the lifetime of the electron–hole in the K-shell. Both the K-edge energy and the edge width increase with the atomic number (Keski-Rahkonen & Krause, 1974). As described in Section 2.1, the K-edge selection must be considered along with the selection of the monochromator crystal. Fig. 5 shows the simulated vertical photon-beam profiles indicating the edge widths that contain contributions from both the monochromator and the filter K-edge. Even though the crystal bandwidth is smaller for the Si(440) crystal (Fig. 4), the total edge width is spatially larger in y (see Fig. 5) because of the increased energy dispersion of the (440) reflection compared with the (111) reflection.

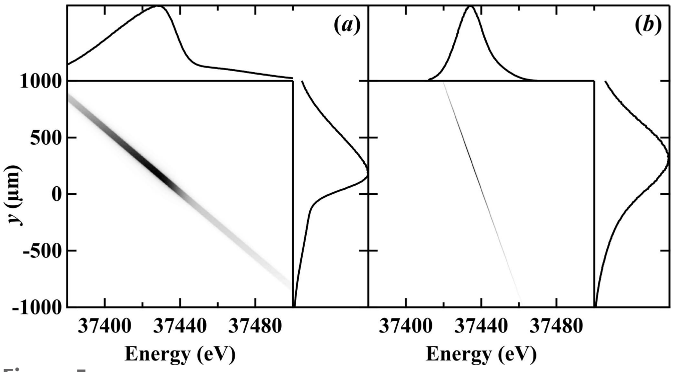

Figure 5
Simulated DuMond diagrams using a zero-emittance BM source that is diffracted by (a) a Si(111) and (b) a Si(440) crystal, and filtered by a barium filter with a finite K-edge width ($\sigma_{E_{K\,\mathrm{edge}}} = 5.6$ eV).

Table 2
The angular width of the monochromator, $\sigma_{y'_{\mathrm{mono}}}$, the projected filter K-edge width, $\sigma_{y'_{K\,\mathrm{edge}}}$, and their total contribution, $\sigma_{y'_{\mathrm{total}}}$, calculated using equation (12).

	E_K (keV)	θ_K (°)	$\sigma_{y'_{\mathrm{mono}}}$ (μrad)	$\sigma_{y'_{K\,\mathrm{edge}}}$ (μrad)	$\sigma_{y'_{\mathrm{total}}}$ (μrad)
Si(111)					
Cu	8.979	12.72	13.4	13.3	18.9
Mo	20.000	5.674	5.8	9.2	10.8
Ag	25.514	4.445	4.5	8.6	9.7
I	33.169	3.418	3.5	8.0	8.7
Ba	37.441	3.027	3.1	7.9	8.5
Si(220)					
Cu	8.979	21.08	10.1	22.8	24.9
Mo	20.000	9.291	4.2	15.1	15.6
Ag	25.514	7.270	3.3	14.1	14.5
I	33.169	5.586	2.5	13.0	13.3
Ba	37.441	4.947	2.2	13.0	13.1
Si(440)					
Cu	8.979	45.99	4.8	61.2	61.4
Mo	20.000	18.84	1.5	31.4	31.5
Ag	25.514	14.66	1.2	29.0	29.0
I	33.169	11.23	0.9	26.4	26.4
Ba	37.441	9.931	0.8	26.2	26.2

Quantitatively, the total contribution from both the monochromator and the K-edge filter add in quadrature as

$$\sigma_{y'_{\mathrm{total}}} = \left(\sigma^2_{y'_{K\,\mathrm{edge}}} + \sigma^2_{y'_{\mathrm{mono}}}\right)^{1/2}. \qquad (12)$$

The calculated $\sigma_{y'_{\mathrm{mono}}}$, $\sigma_{y'_{K\,\mathrm{edge}}}$ and $\sigma_{y'_{\mathrm{total}}}$ values for different filter elements and crystal reflections are summarized in Table 2, where $\sigma_{y'_{\mathrm{mono}}}$ is the fitted Gaussian width of the diffraction profile calculated using *XOP* (Sánchez del Río & Dejus, 2011), and $\sigma_{y'_{K\,\mathrm{edge}}}$ is calculated using equation (11) with $\sigma_{E_{K\,\mathrm{edge}}}$ extracted from Fig. 1 in the work by Babanov *et al.* (1998). As the element atomic number goes up, the total contribution from the K-edge width and monochromator width becomes smaller, which implies a better sensitivity for detecting the electron-source size based on equation (2). Since the total contribution is mostly dominated by the K-edge width, the bandwidth of the monochromator has relatively less effect. Therefore, crystals with lower reflection indices [*i.e.* Si(111)] are preferred because of the smaller Bragg angle. Table 2 also shows that the reduction of the total width is not that dramatic when going to a higher atomic number than iodine. Considering that most of the BM sources have critical energies much less than 30 keV, going to a higher energy leads to a rapid reduction in flux as well. One should therefore choose as high an energy as possible while maintaining sufficient flux.

2.2.2. Filter concentration. The choice of filter concentration and thickness (projected concentration) will affect the sensitivity and accuracy of the source-size measurement. Fig. 6 shows the extracted (a) edge jumps, (b) edge profiles and (c) source sizes calculated with different Ba filter concentra-

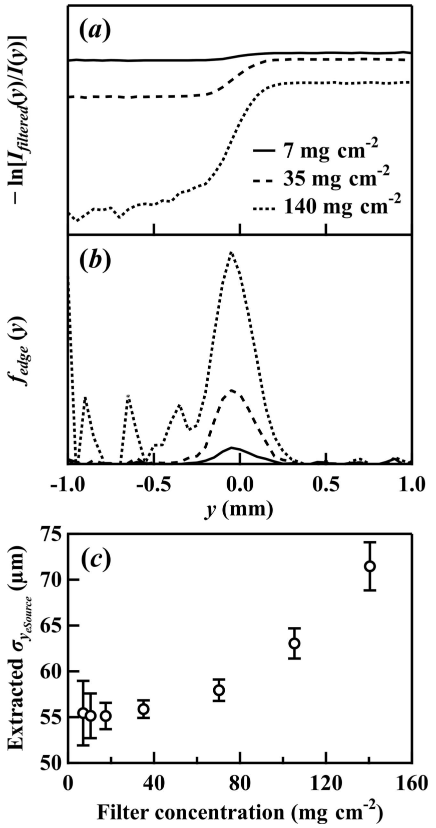

Figure 6
Simulated barium *K*-edge steps (*a*) and *K*-edge profiles (*b*), and the extracted source sizes (*c*) with different filter projected concentrations.

tions. When the filter projected concentration is low (*e.g.* 7 mg cm^{-2}), the absorption-edge contrast is low, which gives a lower intensity edge profile and higher noise level. Therefore, the extracted source sizes have larger uncertainties, shown by the error bars in Fig. 6(*c*). On the other hand, when the filter projected concentration is too high (*e.g.* 140 mg cm^{-2}), the filter absorbs most of the light on the high-energy side (negative *y*-value side) of the spectrum, which tends to broaden the fitted edge width and thus gives a larger source size. The relative fitting error is also large in high filter-projected-concentration cases. As a result, the best filter projected concentration for Ba is around 35 mg cm^{-2}. In practice, it is easy to optimize the filter projected concentration experimentally by analyzing the measurement error and accuracy as demonstrated by the simulation.

2.3. Geometry

The basic geometry of the ps-BPM system is shown in Fig. 1. Other than the obvious arrangement where the system elements must intercept the incident and diffracted beams, the only relevant distance is the source-to-detector distance, *D*, as indicated in equations (1)–(4).

The source-to-detector distance, *D*, must be optimized to maximize the sensitivity of the ps-BPM system. Simulation was carried out using the parameters described in Section 2 with variable distances, *D*. The standard deviation (RMS error) of the simulated electron-source size and position, which is a good measure of the sensitivity of the ps-BPM system, is plotted as a function of *D* in Figs. 7(*a*) and 7(*b*), respectively. The sensitivity for detecting the source position, *y*, is linearly related to the choice of *D* [see Fig. 7(*a*)]. More importantly, the sensitivity for measuring the source size is inversely proportional to D^2 [see Fig. 7(*b*)].

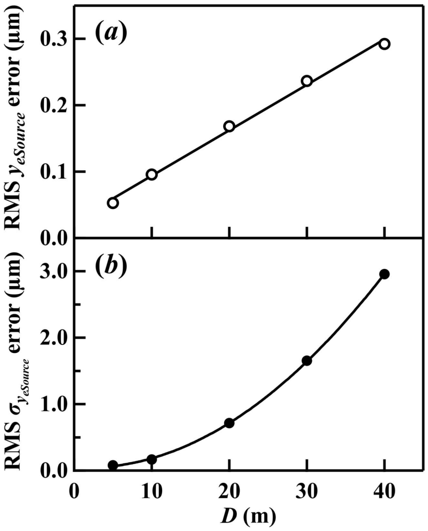

Figure 7
RMS error of the simulated electron-source position (*a*) and size (*b*) as a function of the source-to-detector distance, *D*.

It is therefore beneficial to reduce *D* to optimize the sensitivity of the ps-BPM system. Because of the physical space limitation in a typical beamline, a distance of 10 m would be a reasonable choice for existing or planned BM beamlines that are dedicated to source diagnostics. Another concern of having a short distance is that the quadratic increase of the incident-power density will increase the thermal deformation on the monochromator crystals, which will degrade the accuracy of the size and angle measurements. In that case, an aggressive cooling scheme will be required.

2.4. Detector

The determination of the unfiltered beam location and width as well as the filtered beam *K*-edge location and width relies on curve fitting to the measured $I_0(y)$ and $f_{\rm edge}(y)$ profiles using equations (7) and (8), respectively. The edge width is normally in the range of a few tens of microradians as shown in Table 2. There must also be enough spatial resolution across the edge width to ensure an accurate fitting. Fig. 8 shows the simulated source size and divergence as a function of the pixel size (bin size of the histograms) with the total flux (number of rays) kept constant. A pixel size of a few tens of micrometres is adequate to ensure the accuracy of the source size and divergence measurements. Previous experiments (Samadi *et al.*, 2019) show that a detector with 100 μm pixel size is sufficient to measure third-generation synchrotron source sizes. Overall, the accuracy of the curve-fitting proce-

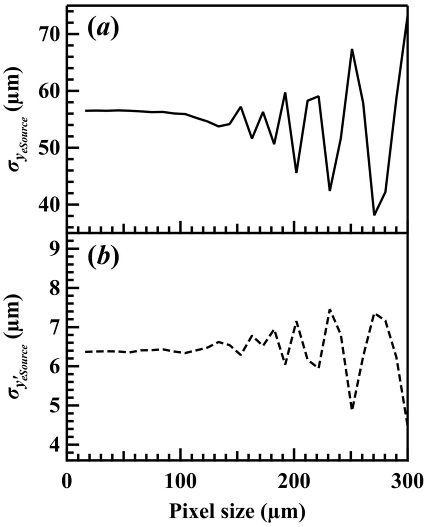

Figure 8
Extracted electron-source size (*a*) and divergence (*b*) as a function of detector pixel size (bin size of the simulated histograms).

dure is more sensitive to the integrated flux than to the pixel size of the detector.

The next-generation synchrotrons have the source size and divergence one order of magnitude smaller. A similar study shows that a pixel size of 10 μm is expected to be sufficient for the APS-U source, assuming perfect detectors. However, the noise level (dark noise and others) on the detector will affect the curve-fitting results and reduce the measurement sensitivity. The smallest measurable size of the ps-BPM system will be limited by the flux, the detector resolution and the noise level, which needs further study.

3. Example of a ps-BPM system for APS-U

Based on all of the above studies, an optimized configuration is proposed for the low-emittance APS-U project. The APS-U will have 42 pm rad natural emittance (Borland *et al.*, 2018). Simulations were performed with the source parameters at the M3 BM with $\sigma_{y_{\rm eSource}}$ = 4.9 μm and $\sigma_{y'_{\rm eSource}}$ = 2.8 μrad, a single-Bragg Si(111) monochromator tuned to the barium *K*-edge energy (37.441 keV), a 35 mg cm^{-2} barium filter, a source-to-detector distance of D = 10 m, and a detector pixel size of 10 μm.

Using the simulation procedure described in Section 1.2, the ability of the ps-BPM to measure the source properties was analyzed. Fig. 9 shows the predicted output source properties as a function of the input values that varied relative to their nominal values by as low as 5%. The source position and angular position were simulated with 5 × 10^7 rays and obtained from equations (1) and (8), and equations (3) and (7), respectively. The source size and divergence were studied with 5 × 10^8 rays and extracted using equations (9) and (10), respectively.

The ps-BPM system has an excellent ability to measure the source position and angular position as shown in Figs. 9(*a*) and 9(*b*). The measurement of source position and angular position is fast and considered real time. The source size and divergence can be extracted at the same time, which is one of the main features of the ps-BPM system. The sensitivity to the source-size variation is about 10% of the nominal source size in these calculations because of the limited statistics. The source-size measurement is the most photon-hungry component of the system. In real measurements, increasing the acquisition time will improve the sensitivity, but with limited measurement speed.

The sensitivity of the ps-BPM system is flux driven, but nonlinearly. The required flux level can only be estimated with the comparison of experimental and simulation results. One feature of *SHADOW* ray-tracing is that rays can have fractional intensities to account for the crystal reflectivity and filter absorption. Therefore, a single ray can represent a large number of photons. From the previous studies (Samadi *et al.*, 2019), simulation with 1 × 10^7 rays gives the same sensitivity as the measurement of source size performed with a flux level of 1.2 × 10^{10} photons Hmrad^{-1} (where H means horizontal) To achieve the sensitivity shown in Fig. 9(*c*), simulation with 5 × 10^8 rays indicates that a flux level of 5.9 × 10^{11} photons Hmrad^{-1} is needed for measuring the APS-U source size.

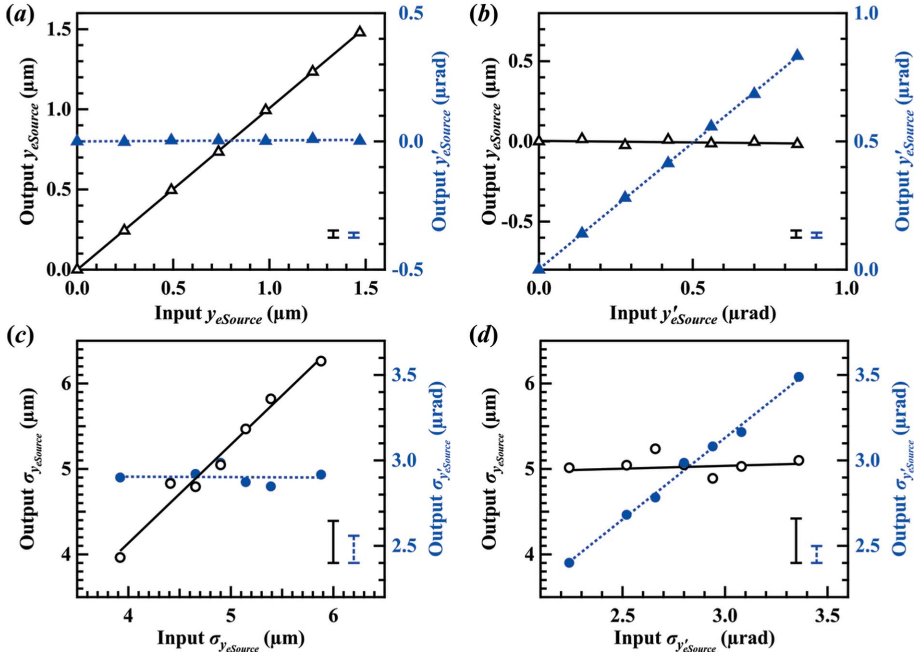

Figure 9
Predicted output electron-source position (open triangles) and angular position (closed triangles) values from different input values of position (*a*) and angular position (*b*). Predicted output electron-source size (circles) and divergence (bullets) values from different input values of size (*c*) and divergence (*d*).

Considering an Si(111) Bragg crystal monochromator with no filter, this requires a minimum of 1.5 s exposure time.

4. Conclusion

The ps-BPM system can precisely measure electron-beam source position and angle, which are relative to the K-edge location in the filtered side of the photon beam as well as the central location of the unfiltered beam. The system can also provide accurate measurements of the electron-source size and divergence from knowledge of the K-edge width and the full photon-beam width. The simultaneous measurement of all four source properties in the vertical plane is a unique feature of the ps-BPM system. In principle, the system can also be used to measure the source position and size in the horizontal plane but a separate horizontally deflecting monochromator will be required.

Factors that affect the sensitivity and resolution of the system include the choice of monochromator, K-edge filter, geometry of the system and detector. The optimized configuration contains low-index crystal reflections, a high-energy K-edge filter and a relatively small source-to-detector distance. The filter-element concentration must be selected to ensure enough absorption contrast while maintaining a reasonable transmission on the high-energy side of the K-edge. Compared with other systems, the ps-BPM monitor has less-demanding requirements on detector resolution, which makes it capable of high-speed measurements.

It is also worth pointing out that the ps-BPM system can measure a wide size range. The larger the source size, the easier (or faster) it can be measured, as long as the source-size contribution ($\sigma_{y_{\rm eSource}}/D$) is smaller than the natural opening angle of the photon beam.

A single-crystal monochromator may generate Compton scatter at the detector location which reduces signal contrast. To achieve a higher sensitivity, the use of a two-crystal monochromator should be considered. Another concern is fluorescence from the K-edge filter, some of which may also provide background in the detector. Other considerations for a practical system include mechanical stability and thermal management of the monochromator.

Simulations validated by measurement show that the ps-BPM system is suitable for next-generation light sources. An optimized system for the APS-U source was presented as an example to demonstrate the performance. The source position and angular motion can be monitored with high precision and at high speed; while the source-size measurement is photon hungry, which creates a trade-off between measurement speed and resolution. Because of the relatively simple configuration of the ps-BPM monitor, it can coexist and operate in parallel with other systems at the same beamline.

Acknowledgements

The authors would like to thank Dr Luca Rebuffi (Argonne National Laboratory) for the *OASYS* support and Dr Les Dallin (Canadian Light Source) for the invaluable discussions.

Funding information

This work was supported by the US Department of Energy, Office of Basic Energy Sciences, under Contract No. DE-AC02-06CH11357, Natural Sciences and Engineering Research Council of Canada (NSERC) Discovery Grant, Canadian Institutes of Health Research (CIHR) Team Grant – Synchrotron Medical Imaging, CIHR Training Grant – Training in Health Research Using Synchrotron Techniques, the Canada Research Chair Program, Saskatchewan Health Research Foundation Team Grant, and the University of Saskatchewan.

References

Andersson, Å., Böge, M., Lüdeke, A., Schlott, V. & Streun, A. (2008). *Nucl. Instrum. Methods Phys. Res. A*, **591**, 437–446.

Babanov, Y. A., Ryazhkin, A. V., Sidorenko, A. F. & Blaginina, L. A. (1998). *J. Struct. Chem.* **39**, 833–838.

Bergstrom, J. C. & Vogt, J. M. (2008). *Nucl. Instrum. Methods Phys. Res. A*, **587**, 441–457.

Borland, M., Abliz, M., Arnold, N., Berenc, T., Byrd, J., Calvey, J., Carter, J., Carwardine, J., Cease, H., Conway, Z., Decker, G., Dooling, J., Emery, L., Fuerst, J., Harkay, K., Jain, A., Jaski, M., Kallakuri, P., Kelly, M., Kim, S. H., Lill, R., Lindberg, R., Liu, J., Liu, Z., Nudell, J., Preissner, C., Sajaev, V., Sereno, N., Sun, X., Sun, Y., Veseli, S., Wang, J., Wienands, U., Xiao, A., Yao, C. & Blednykh, A. (2018). *Proceedings of the Ninth International Particle Accelerator Conference (IPAC'18)*, 29 April to 4 May 2018, Vancouver, Canada, pp. 2872–2877. THXGBD1.

Breunlin, J. & Andersson, Å. (2016). *Proceedings of the Seventh International Particle Accelerator Conference (IPAC'16)*, 8–13 May 2016 Busan, Korea, pp. 2908–2910. WEPOW034.

Corbett, W. J., Huang, X., Wu, J., Li, C. L., Mitsuhashi, T. M., Xu, Y. H. & Zhang, W. J. (2016). *Proceedings of the International Beam Instrumentation Conference (IBIC'16)*, 11–15 September 2016, Barcelona, Spain, pp. 236–239. MOPG70.

DuMond, J. (1937). *Phys. Rev.* **52**, 872–883.

Einfeld, D., Plesko, M. & Schaper, J. (2014). *J. Synchrotron Rad.* **21**, 856–861.

Elleaume, P., Fortgang, C., Penel, C. & Tarazona, E. (1995). *J. Synchrotron Rad.* **2**, 209–214.

Eriksson, M., van der Veen, J. F. & Quitmann, C. (2014). *J. Synchrotron Rad.* **21**, 837–842.

Keski-Rahkonen, O. & Krause, M. O. (1974). *At. Data Nucl. Data Tables*, **14**, 139–146.

Mitsuhashi, T. (1999). *Beam Measurement: Proceedings of the Joint US-CERN-Japan-Russia School on Particle Accelerators*, edited by S. Kurokawa, S. Y. Lee, E. Perevedentsev & S. Turner, 11–20 May 1998, Montreux and Geneva, Switzerland, pp. 399–427. Singapore: World Scientific.

Naito, T. & Mitsuhashi, T. (2006). *Phys. Rev. ST Accel. Beams*, **9**, 122802.

Rebuffi, L. & Sánchez del Río, M. (2016). *J. Synchrotron Rad.* **23**, 1357–1367.

Rebuffi, L. & Sanchez del Rio, M. (2017). *Proc. SPIE*, **10388**, 103880S.

Renner, T. R., Padmore, H. A. & Keller, R. (1996). *Rev. Sci. Instrum.* **67**, 3368.

Samadi, N., Bassey, B., Martinson, M., Belev, G., Dallin, L., de Jong, M. & Chapman, D. (2015). *J. Synchrotron Rad.* **22**, 946–955.

Samadi, N., Shi, X., Dallin, L. & Chapman, D. (2019). *J. Synchrotron Rad.* **26**, 1213–1219.

Sánchez del Río, M. & Dejus, R. J. (2011). *Proc. SPIE*, **8141**, 814115.

Sanchez del Rio, M., Perez-Bocanegra, N., Shi, X., Honkimäki, V. & Zhang, L. (2015). *J. Appl. Cryst.* **48**, 477–491.

Schwinger, J. (1949). *Phys. Rev.* **75**, 1912–1925.

Tavares, P. F., Leemann, S. C., Sjöström, M. & Andersson, Å. (2014). *J. Synchrotron Rad.* **21**, 862–877.

Thomas, C., Rehm, G., Martin, I. & Bartolini, R. (2010). *Phys. Rev. ST Accel. Beams*, **13**, 022805.

Warren, B. E. (1969). *X-ray Diffraction*. Reading, Massachusetts, USA: Addison-Wesley.

Zachariasen, W. H. W. (1945). *Theory of X-ray Diffraction in Crystals*. New York: John Wiley.

Zhu, D., Yue, J., Sui, Y. & Cao, J. (2018). *Proceedings of the Ninth International Particle Accelerator Conference (IPAC'18)*, 29 April to 4 May 2018, Vancouver, Canada, pp. 2151–2154. WEPAL005.